Optical coherence properties of Kramers' rare-earth ions at the nanoscale for quantum applications

Mohammed K. Alqedra,[1,*] Chetan Deshmukh,[2,*] Shuping Liu,[3,4] Diana Serrano,[3] Sebastian P. Horvath,[1] Safi Rafie-Zinedine,[1] Abdullah Abdelatief,[1] Lars Rippe,[1] Stefan Kröll,[1] Bernardo Casabone,[2] Alban Ferrier,[3,5] Alexandre Tallaire,[3] Philippe Goldner,[3] Hugues de Riedmatten,[2,6] and Andreas Walther[1]

[1]*Department of Physics, Lund University, P.O. Box 118, SE-22100 Lund, Sweden*

[2]*ICFO-Institut de Ciencies Fotoniques, The Barcelona Institute of Science and Technology, 08860 Castelldefels, Barcelona, Spain*

[3]*Chimie ParisTech, PSL University, CNRS, Institut de Recherche de Chimie Paris, 75005 Paris, France*

[4]*Shenzhen Institute for Quantum Science and Engineering, Southern University of Science and Technology, 518055 Shenzhen, China*

[5]*Faculté des Sciences et Ingénierie, Sorbonne Université, UFR 933, 75005 Paris, France*

[6]*ICREA-Institució Catalana de Recerca i Estudis Avaçats, 08015 Barcelona, Spain*

(Received 6 March 2023; revised 13 July 2023; accepted 24 July 2023; published 3 August 2023)

Rare Earth (RE) ion doped nanomaterials are promising candidates for a range of quantum technology applications. Among RE ions, the so-called Kramers' ions possess spin transitions in the GHz range at low magnetic fields, which allows for high-bandwidth multimode quantum storage, fast qubit operations as well as interfacing with superconducting circuits. They also present relevant optical transitions in the infrared. In particular, Er^{3+} has an optical transition in the telecom band, while Nd^{3+} presents a high-emission-rate transition close to 890 nm. In this paper, we measure spectroscopic properties that are of relevance to using these materials in quantum technology applications. We find the inhomogeneous linewidth to be 10.7 GHz for Er^{3+} and 8.2 GHz for Nd^{3+}, and the excited state lifetime T_1 to be 13.68 ms for Er^{3+} and 540 μs for Nd^{3+}. We study the dependence of homogeneous linewidth on temperature for both samples, with the narrowest linewidth being 379 kHz ($T_2 = 839$ ns) for Er^{3+} measured at 3 K, and 62 kHz ($T_2 = 5.14$ μs) for Nd^{3+} measured at 1.6 K. Further, we investigate time-dependent homogeneous linewidth broadening due to spectral diffusion and the dependence of the homogeneous linewidth on magnetic field to get additional clarity of mechanisms that can influence the coherence time. In light of our results, we discuss two applications: single qubit-state readout and a Fourier-limited single photon source.

DOI: 10.1103/PhysRevB.108.075107

I. INTRODUCTION

Rare Earth (RE) ions doped into inorganic crystals have been widely investigated as a solid-state platform for quantum applications, including quantum memories [1–4], quantum information processors [5–8], quantum sensors [9,10], and microwave-to-optical transducers [11,12]. This interest is mainly motivated by the exceptionally long optical and spin coherence times of the *4f-4f* transitions at cryogenic temperatures. Other motivations include the highly dense spectral storage capabilities, which are facilitated by narrow homogeneous lines (kHz) spread over much wider inhomogeneous lines (GHz). This allows the different frequency channels to be used to address the spin states of different ions, even though they can be within nanometers of each other, giving a high potential qubit density [13–15]. High-fidelity detection of single RE ions is important for several applications, such as quantum networks and quantum computing [16,17]. However, the low spontaneous emission rate of RE ions resulting from the dipole-forbidden nature of the *4f-4f* transitions makes this very challenging.

During the last few years, single RE ion detection has been demonstrated by Purcell enhancing the weak *4f* transitions using different types of cavities [18–22]. To incorporate RE ion doped crystals into small mode-volume optical cavities, nanostructuring of the host crystal is essential. In this regard, yttrium oxide (Y_2O_3) has emerged as a very promising host material due to the excellent coherence properties that RE ions doped into nanoscale Y_2O_3 have demonstrated [23–27]. Recently, RE ions doped into Y_2O_3 nanoparticles were also coupled to high-finesse fiber-based microcavities to demonstrate Purcell-enhanced emission [22,28].

Among RE ions, so-called Kramers' ions with an odd number of *4f* electrons, including erbium (Er^{3+}), neodymium (Nd^{3+}), or ytterbium (Yb^{3+}), offer unique possibilities due to their high magnetic-moments. Their spin transitions can be tuned in the GHz range even at low magnetic fields, which can be used for high-bandwidth multimode quantum storage [29,30], fast qubit operations [19,31], and for interfacing with superconducting qubits [32,33].

In this paper, we investigate two of the most appealing Kramers' ions for quantum applications, Er^{3+} and Nd^{3+}. The ${}^4I_{13/2} - {}^4I_{15/2}$ transition in Er^{3+} at 1.5 μm lies in the telecommunication band, and hence offers easy integration into existing commercial fiber-optic networks for the purpose of

[*]These authors contributed equally to this work.

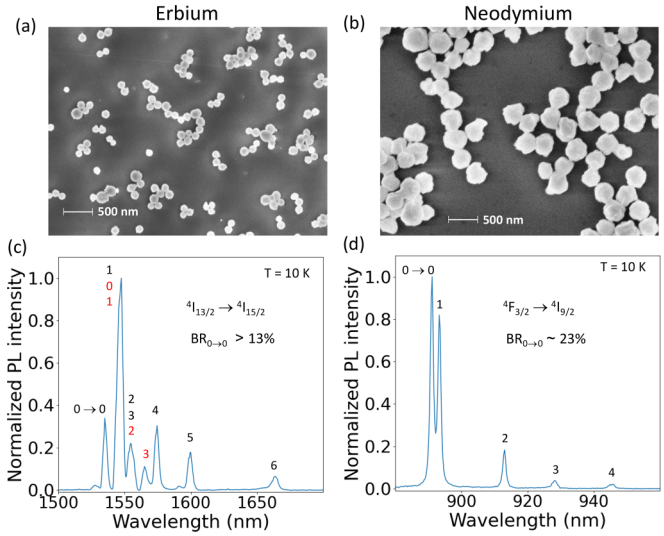

FIG. 1. (a) Scanning electron microscopy (SEM) image of Er^{3+} : Y_2O_3 nanoparticles with average size of 150 ± 13 nm and of (b) Pr^{3+}–Nd^{3+} : Y_2O_3 nanoparticles with average size of 380 ± 24 nm. (c) Fluorescence spectra of Er^{3+} : Y_2O_3 at 10 K on the $^4I_{13/2} - {}^4I_{15/2}$ transition obtained by exciting the $^4I_{11/2}$ level at 975 nm. The different peaks in the spectra were assigned to transitions from the lowest energy level in the $^4I_{13/2}$ multiplet to the different energy levels in the ground-state multiplet ($^4I_{15/2}$) for both site 1 (black) and site 2 (red). Peaks at 1548 nm and 1555 nm contain several unresolved emission lines. We estimate a lower bound branching ratio of 13% for the $0 \rightarrow 0$ line, at 1535 nm. (d) Pr^{3+}–Nd^{3+} : Y_2O_3 on the $^4F_{3/2} - {}^4I_{9/2}$ transition obtained by exciting the $^4F_{5/2}$ level at 813 nm, where we measure a branching ratio of 23% for the $0 \rightarrow 0$ line at 892 nm.

quantum communication. The $^4F_{3/2} - {}^4I_{9/2}$ transition in Nd^{3+} has one of the highest oscillator strengths among all RE ions and a high branching ratio, which together make it very promising to achieve high cooperativity in an optical cavity [34,35].

In this paper, we experimentally characterize the optical spectroscopic properties of the $^4I_{13/2} - {}^4I_{15/2}$ transition in Er^{3+} and of the $^4F_{3/2} - {}^4I_{9/2}$ transition in Nd^{3+} doped into Y_2O_3 nanoparticles. In Sec. III A, we report excited state lifetimes (T_1) as well as inhomogeneous linewidths. In Sec. III B, we characterize Er^{3+} and Nd^{3+} homogeneous linewidths as a function of temperature. In Sec. III C, we measure time-dependent spectral diffusion in Er^{3+}. In Sec. III D, we investigate the dependence of homogeneous linewidth of Nd^{3+} on magnetic field. Finally, in light of our results, we present an outline for two possible quantum applications in Sec. IV, namely, Fourier-limited single photon sources and single qubit state readout.

II. EXPERIMENT

A. Material

Two batches of Y_2O_3 nanoparticles were investigated in this paper: one doped with Er^{3+} (200 ppm at.), presenting an average particle size of 150 nm, and a second one codoped with Nd^{3+} (100 ppm at.) and Pr^{3+} (500 ppm at.) ions, presenting average particle size of 380 nm [Figs. 1(a) and 1(b)]. The nanoparticles were obtained by homogeneous precipitation followed by high-temperature annealing. The synthesis route is described in full detail in Refs. [24,36]. The annealing temperature was set to 900 °C for 6 h for the Er^{3+} sample while it was 1200 °C for 6 h in the Nd^{3+}–Pr^{3+} one. A lower temperature was used for Er^{3+} to avoid aggregation during annealing due to the nanoparticles' reduced size. In addition, Er^{3+} nanoparticles were processed under pure O_2 plasma twice for three minutes to cure defects [24]. Particle size, morphology, and dispersion were assessed by scanning electron microscopy [Figs. 1(a) and 1(b)]. The microstructure of the nanoparticles was determined by x-ray diffraction (XRD) analysis using the Williamson-Hall method, as polycrystalline, with crystallites of 58 ± 11 nm for Er^{3+} and 102 ± 10 nm for Nd^{3+}–Pr^{3+} Y_2O_3. The latter also confirms that the nanoparticles present a pure cubic phase with Ia-3 space group (JCPDS 01-080-6433). In this structure, RE ions occupy two different crystal sites, with C_2 and S_6 point symmetries, respectively, and can be distinguished by their different $0 \rightarrow 0$ transition frequencies [37]. In this paper, we will investigate spectroscopic properties of Er^{3+} and Nd^{3+} ions in C_2 sites.

Y_2O_3 ceramics doped with Er^{3+} (200 ppm at.) and Nd^{3+} (100 ppm at.) were also synthesized by solid-state reaction to be used as bulk references. Those were fabricated from a mix of commercial Y_2O_3 and Er_2O_3 (or Nd_2O_3) oxide powders (with 99.99% purity). The powders were pressed into pellets with a pressure of 5 MPa, and then annealed at 1500 °C for 48 h in an air atmosphere. The obtained ceramics were cut into thin slabs ~260 μm thick for the optical measurements.

B. Procedures

For measurements on Er^{3+}, the transition of interest is $^4I_{13/2}(0) - {}^4I_{15/2}(0)$ at around 1535 nm, which lies in the telecom band. The excitation light was obtained from an external cavity diode laser at 1535 nm, which was then amplified by an erbium-doped fiber amplifier to reach a peak power of ~500 mW. The amplified light was sent through a double-pass acousto-optic modulator (AOM) for pulse modulation. The light was then filtered with a bandpass filter at 1535 ± 3 nm before being focused onto the sample using a 35 mm spherical lens. Typical peak power at the sample was ~150 mW. The samples were prepared on a copper holder with a pinhole and placed on the cold finger of a closed-cycle cryostat, which was cooled down to a minimum of 3 K. The temperature of the sample could be increased with the help of heaters installed on the cold finger. The scattered light after the sample was then loosely focused onto an avalanche photodiode (APD) with the help of two spherical lenses, each with a focal length of 60 mm. The signal from the APD was recorded on an oscilloscope. For two-pulse photon echo (2PPE) measurements, the two pulses had a duration of 250 ns in length, and the delay between them was varied from 150 ns to 3 μs. For three-pulse photon echo (3PPE) measurements, all three pulses were 250 ns, and the delay between the first two pulses was kept constant at 150 ns while the delay between the second and third pulse was varied from 3 μs to 40 μs. A heterodyne scheme was used to detect the echo where the heterodyne pulse was 1 μs long with a frequency

detuning of 24 MHz. The resulting beat note signal from the APD was recorded on an oscilloscope after passing through a high-pass filter with a cutoff frequency of ∼5 MHz to filter out electronic noise. A small magnetic field of ∼100 G was applied for all of the measurements with the help of permanent magnets.

For measurements on Nd^{3+}, a CW Ti:sapphire laser operating at a wavelength of 892 nm was used to target the ${}^4F_{3/2}(0) - {}^4I_{9/2}(0)$ transition. A double pass AOM was also utilized for pulse shaping. To calibrate for laser intensity fluctuations, 10% of the input was focused into a reference detector before the sample. The rest of the light, which amounted to ∼10 mW, was focused on the sample. A copper mount was used to hold the sample inside a bath cryostat operating at 2.15 K. The cryostat was equipped with a superconducting magnet system that can reach up to 7 T. For the temperature dependence measurement, the cryostat was configured to cool using helium exchange gas. The scattered light after the sample was collected and focused onto an APD. For inhomogeneous line and lifetime measurements, a 900 nm long-pass filter was mounted before the detector to filter out the excitation light while passing part of the fluorescence emission [see Fig. 1(d)]. For coherence measurements, a 2PPE sequence was used with 400-ns-long pulses and direct echo detection.

Low-temperature emission spectra shown in Figs. 1(c) and 1(d) were recorded at 10 K using a closed-cycle cryostat. Excitation was carried out with a tunable optical parametric oscillator pumped by a Nd^{3+}:YAG Q-switched laser (Ekspla NT342BSH with 6 ns pulse length and 10 Hz repetition rate). Spectra were recorded using an Acton SP2300 spectrometer equipped with the following visible and infrared gratings: 300 grooves/mm centered at 1200 nm, 300 grooves/mm centered at 500 nm, and 600 grooves/mm centered at 1.2 μm. An ICCD camera (Princeton Instruments) and a Ge detector were used to detect Nd^{3+} and Er^{3+} emissions, respectively. For Er^{3+}, the excitation wavelength was set to 975 nm while emissions from the ${}^4I_{13/2} - {}^4I_{15/2}$ transition were collected. We note that the spectrum in Fig. 1(c) contains lines from both C_2 and S_6 sites. We estimate a branching ratio >13% on the $0 \rightarrow 0$ line for Er^{3+} ions in C_2, with the 0 denoting the lowest crystal field level of a given J multiplet. This is, however, a lower bound value as not all S_6 emission lines could be resolved from that of C_2. For Nd^{3+}, the excitation wavelength was set to 813 nm while the collection was carried out between 880 and 940 nm on the ${}^4F_{3/2} - {}^4I_{9/2}$ transition. We estimate a branching ratio of 23% for the $0 \rightarrow 0$ line from the spectrum in Fig. 1(d), taking into account the branching ratio for the ${}^4F_{3/2} - {}^4I_{9/2}$ transition given in the literature [38]. In contrast to Er^{3+}, there is no emission from Nd^{3+} ions in S_6 sites in Y_2O_3.

III. RESULTS

A. Inhomogeneous linewidth and lifetime

The optical inhomogeneous lines for all the samples are shown in Figs. 2(a) and 2(b). For $Er^{3+} : Y_2O_3$, the center of the inhomogeneous line in the ceramic sample was found to be at 1535.43 nm with a linewidth of 3.98 GHz, while in the nanoparticles the line was redshifted to 1535.48 nm, with a linewidth of 10.7 GHz. This goes along with a tensile strain of 2.3×10^{-4} derived from the Williamson-Hall analysis for

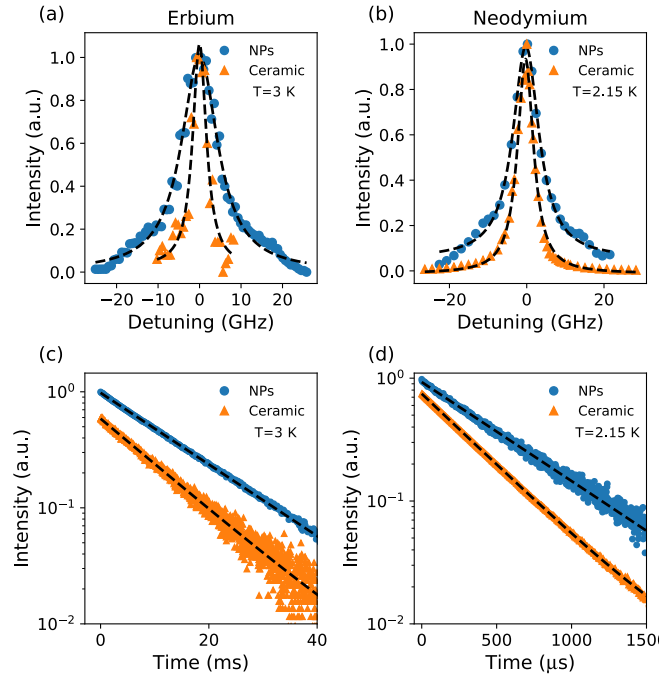

FIG. 2. Inhomogeneous linewidth of the $0 \rightarrow 0$ line of (a) Er^{3+} was measured to be 3.98 GHz in ceramic (orange triangles) and 10.7 GHz in nanoparticles (blue circles); and that of (b) Nd^{3+} was measured to be 5.03 GHz in ceramic (orange triangles) and 8.20 GHz in nanoparticles (blue circles). Lifetime of the excited state of (c) $Er^{3+} : Y_2O_3$ was measured to be 10.91 ms in ceramic (orange triangles) and 13.68 ms in nanoparticles (blue circles); and that of (c) Nd^{3+} was measured to be 373 μs in ceramic (orange triangles), and 540 μs in nanoparticles (blue circles).

$Er^{3+} : Y_2O_3$ nanoparticles. The observed tensile strain and spectral redshift here could be due to the lower annealing temperature applied to the sample (900 °C), as lower temperatures are often less efficient in curing oxygen-vacancy-type defects [24]. For $Nd^{3+} : Y_2O_3$, the center of the inhomogeneous line in the ceramic sample was found to be at 892.17 nm with a linewidth of 5 GHz, while in the nanoparticles the line shows a blueshift to 892.16 nm, with a linewidth of 8.2 GHz. XRD spectrum analysis shows a small compressive strain of -2.5×10^{-5} in this case. The codoping with Pr^{3+} (500 ppm), present in the nanoparticles sample while not in the ceramic, is in most likelihood responsible for the small blueshift and compressive strain. The codoping can also explain the broadening of the inhomogeneous linewidth in the Pr^{3+}–$Nd^{3+} : Y_2O_3$ nanoparticles [39]. For the $Er^{3+} : Y_2O_3$ nanoparticles, the broadening is again most likely related to a larger amount of defects in the sample associated to the lower annealing temperature and additional O_2 plasma processing [24].

Figures 2(c) and 2(d) show excited state lifetime measurements for all samples. For $Er^{3+} : Y_2O_3$, the excited state lifetime measured at 3 K was found to be 10.91 ms in ceramic and 13.68 ms in nanoparticles, while for $Nd^{3+} : Y_2O_3$ at 2.15 K it was 373 μs in the ceramic and 540 μs in the codoped nanoparticles. The reduction of the spontaneous emission rate in the nanoparticles compared to ceramic can be explained by the reduction of the effective refractive index surrounding the nanoparticle samples. This agrees with previous work where

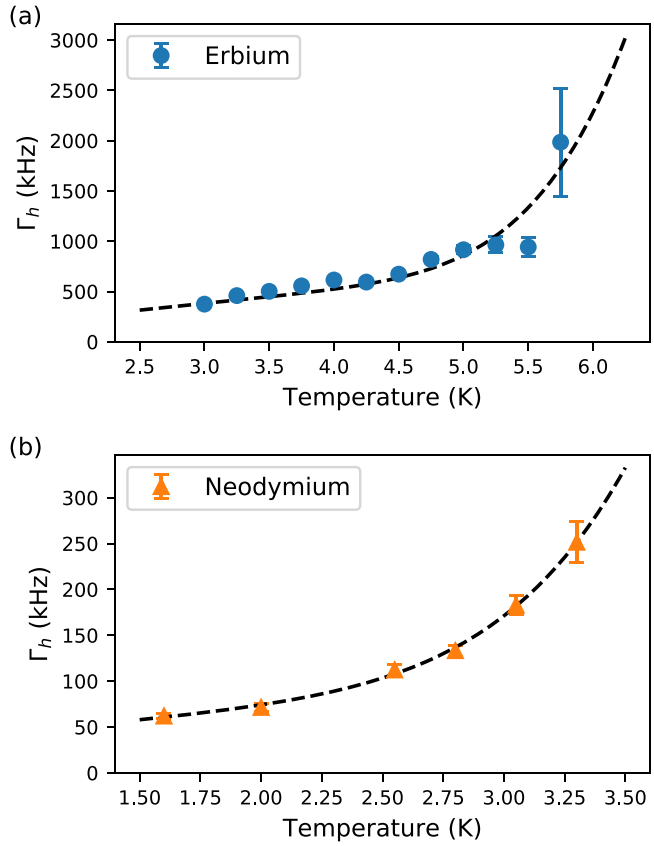

FIG. 3. (a) Homogeneous linewidth of $Er^{3+}:Y_2O_3$ nanoparticles measured as a function of temperature at a magnetic field of 100 G. Dashed line is a fit to Eq. (1) that gives $\Gamma_0 = 9.8$ kHz, $\alpha_{TLS} = 121.7$ kHz/K, and $\alpha_M = 11$ GHz. (b) Homogeneous linewidth of Nd^{3+} in Pr^{3+}–$Nd^{3+}:Y_2O_3$ nanoparticles measured as a function of temperature at zero magnetic field. Fit to Eq. (2) gives an upper bound of 34 kHz for Γ_0, $\alpha_{TLS} = 40$ kHz/K, and $\alpha_M = 2.7$ Hz/K^9. Error bars represent 95% confidence interval obtained from the fit.

an increase in the spontaneous emission rate of Eu^{3+}-doped nanoparticles was found when it was embedded in a PMMA layer as compared to no embedding [22,36].

B. Homogeneous linewidth versus temperature

The homogeneous linewidth of all samples was measured by recording the echo decay in a 2PPE sequence (see Sec. II B for details). For Er^{3+}, we measured a homogeneous linewidth of 68 kHz ($T_2 = 4.65$ µs) in the ceramic sample, while for nanoparticles it was 379 kHz ($T_2 = 839$ ns), both at a temperature of 3 K and a magnetic field of 100 G. This indicates that dephasing in the nanoparticles is dominated by defects and surface related noise as seen in Eu^{3+}-doped nanoparticles [24,27]. We then investigated the dependence of the homogeneous linewidth as a function of temperature, as shown in Fig. 3(a). For $T < 4.5$ K, a linear behavior is observed, evidencing interactions of Er^{3+} ions with two-level systems (TLSs), which are thought to be due to residual disorder in nanocrystals [27]. At higher temperatures, a stronger temperature dependence takes place. It can be due to changes in ground or excited state populations by one-phonon absorption or spin-lattice relaxation (SLR), magnetic noise, or elastic Raman scattering (ERS) acting directly on the optical transition [36]. In the temperature range considered, the dominant Er^{3+} SLR is expected to be an Orbach process associated with crystal field splittings between lowest levels ΔE of 39 and 31 cm^{-1} for the ground and excited multiplets, respectively [40]. Assuming that magnetic noise is due to Er^{3+} ground-state spins themselves, all temperature-dependent contributions to Γ_h thus exhibit an exponential behavior except for the ERS one which is proportional to T^7 at low temperatures [41]. Experimental Γ_h values could be fitted to the expression

$$\Gamma_h(T) = \Gamma_0 + \alpha_{TLS} T + \alpha_{ERS} T^7 + \frac{\alpha_M}{\exp\left(\frac{\Delta E}{k_B T}\right) - 1}, \quad (1)$$

where k_B is the Boltzmann constant. With $\Delta E = 39$ cm^{-1}, we obtained $\Gamma_0 = 9.8$ kHz, $\alpha_{TLS} = 121.7$ kHz/K, and $\alpha_M = 11$ GHz, with a negligible contribution from α_{ERS}. As spin lifetimes of tens of µs can be estimated from $Er:Y_2SiO_5$ parameters at 5 K [42], which corresponds to homogeneous broadening of 10s of kHz only, we attribute the second term of Eq. (1) to magnetic noise driven by Er^{3+} ground-state spin relaxation.

For Nd^{3+} in the codoped particles, we measured a homogeneous linewidth of 62 kHz ($T_2 = 5.14$ µs) for nanoparticles at a temperature of 1.6 K with no magnetic field. The narrower linewidth compared to the Er^{3+}-doped particles is attributed to the Nd^{3+} larger particle size and higher annealing temperature which decrease broadening related to defects [24]. This leads to Γ_h values for Nd^{3+} similar to those measured in Eu^{3+}-doped particles synthesized under similar conditions [27]. Temperature dependence of the homogeneous linewidths in the 1.6–3.25 K range is presented in Fig. 3(b). Its analysis followed the one presented above for Er^{3+} nanoparticles, since Pr^{3+} is nonparamagnetic and should not have a significant effect of Nd^{3+} homogeneous broadening. However, as the maximum investigated temperature was only 3.25 K compared to Nd^{3+} ground and excited splittings of 29 and 196 cm^{-1} (20 and 135 K respectively), SLR should be dominated by a two-phonon Raman process proportional to T^9 [43] and one-phonon absorption negligible. Moreover, the ERS term at low temperatures should also be negligible [27]. Best fits to the data were obtained using the equation

$$\Gamma_h(T) = \Gamma_0 + \alpha_{TLS} T + \alpha_M T^9, \quad (2)$$

and gave an upper bound for Γ_0 of 34 kHz, $\alpha_{TLS} = 40$ kHz/K, and $\alpha_M = 2.7$ Hz/K^9. α_{TLS} is smaller than that for Er^{3+} nanoparticles, suggesting a reduced concentration in structural defects, likely to be also due to Nd^{3+} nanoparticles larger size and annealing temperature.

C. Spectral diffusion in erbium nanoparticles

We now investigate spectral diffusion in $Er^{3+}:Y_2O_3$ nanoparticles via the 3PPE technique, which allows us to probe the broadening of the homogeneous linewidth on a timescale that is much longer than the coherence time. To quantify the broadening Γ_{eff} as a function of time, we keep the separation between the first two pulses in the 3PPE technique t_{12} constant at 150 ns, while varying the separation between pulses two and three t_{23} from 3 µs to 40 µs. The decay of the

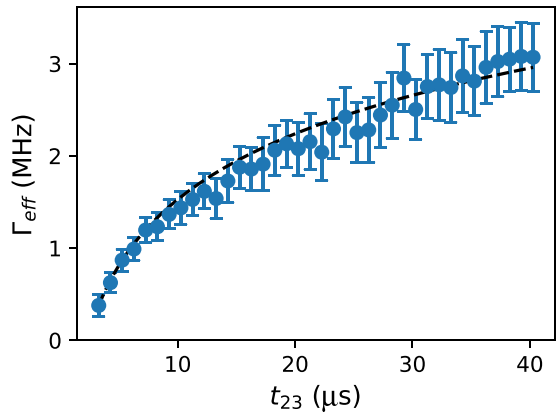

FIG. 4. Effective homogeneous linewidth of $Er^{3+}:Y_2O_3$ nanoparticles as a function of t_{23} in a three-pulse photon echo sequence. Dashed line is a fit to Eq. (4), giving $\Gamma(t_0) = 379$ kHz and $\gamma = 2.3$ MHz. Error bars are one standard deviation of parameter estimate from fit.

echo amplitude in such a 3PPE technique is given by [44]

$$E = E_0 \exp\left(\frac{-t_{23}}{T_1}\right) \exp(-2t_{12}\pi\Gamma_{\text{eff}}), \tag{3}$$

where T_1 is the excited state lifetime. We have $T_1 = 13.68$ ms (as measured above), and $3\,\mu\text{s} \leqslant t_{23} \leqslant 40\,\mu\text{s}$. Hence, the first factor is negligible for our parameters and all decay in echo amplitude is expected to come from a broadening of Γ_{eff}. We begin by recording the decay in the echo amplitude as a function of t_{23}. For the first point of $t_{23} = 3\,\mu$s, we set Γ_{eff} to the value of Γ_h that was obtained from the 2PPE technique, that is, $\Gamma_{\text{eff}} = 379$ kHz. By estimating the relative decay in echo amplitude for all subsequent t_{23}, we extract Γ_{eff} as a function of t_{23} that is shown in Fig. 4. For systems coupled to TLSs, the Γ_{eff} is expected to have the following behavior [45]:

$$\Gamma_{\text{eff}}(t_{12}, t_{23}) = \Gamma(t_0) + \gamma_{sd} \log_{10}\left(\frac{t_{23}}{t_0}\right), \tag{4}$$

where t_0 is the minimum value of $t_{12} + t_{23}$, $\Gamma(t_0)$ is the homogeneous linewidth at t_0, and γ_{sd} is a coupling coefficient. For our case, $t_0 \approx 3\,\mu$s and $\Gamma(t_0) = 379$ kHz. Fitting the Γ_{eff} that we obtained above to Eq. (4), we obtain $\gamma_{sd} = 2.3$ MHz. This is a relatively high value for γ_{sd}. For instance, Veissier *et al.* [45] measured $\gamma_{sd} = 0.4$ MHz for an erbium-doped fiber at a temperature of 0.7 K. Further studies of spectral diffusion as a function of temperature are needed to investigate this.

D. Homogeneous linewidth versus magnetic field in neodymium nanoparticles

Kramers' ions with electron spin could be more sensitive to applied magnetic fields than other ions, so for quantum applications the T_2 dependence of the magnetic field is of relevance. Coherence measurements were taken at different magnetic fields for Nd^{3+} nanoparticles. In Fig. 5(a), the echo area is plotted versus the magnetic field and a clear modulation can be seen on the echo decays when certain magnetic fields are applied. To extract the coherence time and the modulation frequency, the echo decays were fitted to the following

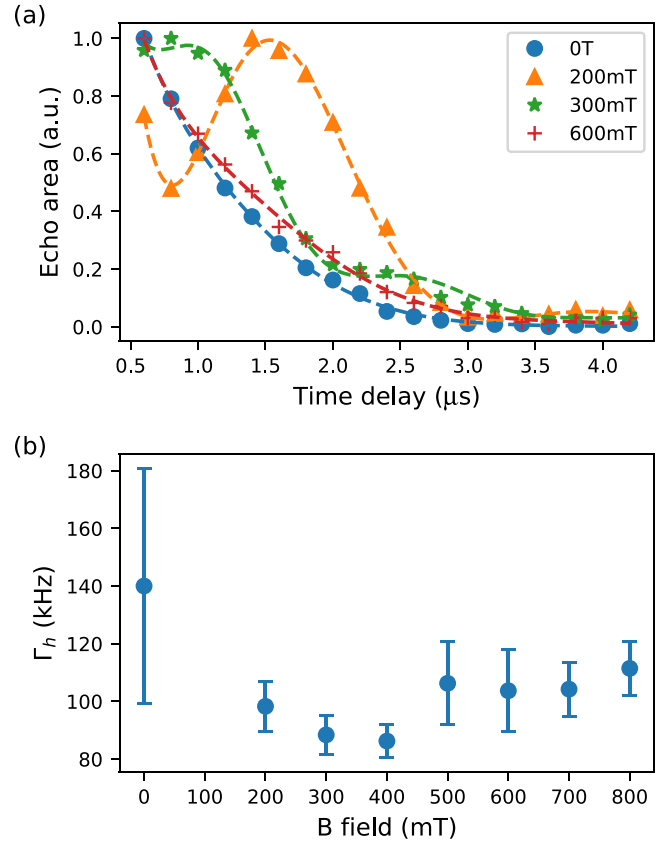

FIG. 5. (a) Photon echo decay at 0 T (blue), 200 mT (red), 300 mT (green), and 600 mT (magenta) measured in Nd^{3+} nanoparticles. Magnetic field dependence of the optical homogeneous linewidth. Error bars represent 95% confidence interval obtained from the fit.

equation [26]:

$$I(t) = I \times e^{(-4t/T_2)} \times [1 + (m \times \cos^2(\omega t/2))]^2, \tag{5}$$

where T_2 is the optical coherence time, m is the modulation amplitude, and ω is the modulation frequency.

The magnetic field dependence of the optical Γ_h is shown in Fig. 5(b). The modulation frequency ranges between 200–900 kHz. Similar modulation has been measured by Zhong *et al.* in $Nd^{3+}:YVO_4$, and was attributed to superhyperfine interaction between the Nd^{3+} electronic spin and the surrounding Y^{3+} nuclear spin [20]. As can be seen in the echo decay plots in Fig. 5(a), no modulation was observed at 0 T, which leads to the high error bars of the fit parameters. While the superhyperfine modulation is strongly dependent on the magnitude of the magnetic field, as predicted by the Hamiltonian described in the Supplemental Material of Ref. [20], no increase in the modulation frequency was observed after 400 mT due to the limited sampling. The saturation of the homogeneous linewidth, Γ_h, around 100 kHz in Fig. 5(b) can be attributed to the superhyperfine limit, where the dephasing is defined by the interaction between Nd^{3+} and the surrounding yttrium nuclei [34,46,47]. Since the Nd^{3+} ion has a large magnetic moment, it creates a frozen core of the low magnetic moment Y^{3+} ions, which as a result slows down their spin-flip rate. The fact that the homogeneous linewidth is relatively unaffected as the field increases is an indication

of the superhyperfine limit since the magnetic noise of Y^{3+} is independent of the applied field [25]. Another effect that could contribute to such saturation is the tunneling TLSs [25,48], which causes fluctuations in the local environment leading to some dephasing. The results show that the optical homogeneous linewidth is relatively unaffected by magnetic fields and, in particular, remains reasonably narrow at zero magnetic field. This is favorable since it allows quantum applications to potentially run without magnetic field, simplifying the setup and avoiding level splitting of other species like qubit ions.

IV. APPLICATIONS

A. Single qubit state readout

Scalability in quantum computers (QCs) necessitate a fast and high fidelity detection of single qubit states. This is challenging for QC schemes based on RE ions due to its naturally forbidden electric dipole transitions. However, there have been several attempts recently to utilize the Purcell enhancement effect to detect single RE ions [19–21,28]. With high enough enhancement, one can either directly detect the qubit state or use a different neighboring ion as a readout qubit [19,21,49]. To avoid any decay of the qubit excited state due to cavity enhancement, we are considering the second approach for the discussion below. In this approach, one can detect the state of a qubit ion that is close to the readout ion, by exciting one of the spin qubit states to the optically exited state. This will shift the levels of the readout ion (or not if the other state was instead populated), using the dipole blockade mechanism [49]. This means that state detection can be made by separating the photon counts for ion emitting versus not emitting (only background). To ensure that the readout time is not a limiting factor in terms of QC speed, the readout should take place on a timescale comparable to the timescale of the gate operation. Typical duration of proposed gate operations in RE systems is in the order of a few microseconds [50]. Furthermore, the homogeneous linewidth of the readout ion, which becomes broader for a shorter lifetime, should be narrower than the frequency shift attained due to the dipole-dipole interaction with the neighboring qubit ion to be detected. This is necessary to obtain high contrast in the photon counts when reading the two-qubit states.

To see how the parameters measured in this paper affects the capacity of our system to read out a QC, we consider our current Pr^{3+}–Nd^{3+} : Y_2O_3 system with Pr^{3+} (500 ppm) as qubit and Nd^{3+} (100 ppm) as a candidate readout ion. We then discuss an ideal system with Eu^{3+} as qubit.

The shift of a transition frequency of one ion, $\Delta\nu_{ij}$, due to the excitation of a neighboring ion via dipole-dipole interaction is given by the following equation [51]:

$$\Delta\nu_{ij} = \frac{\Delta\mu_i \Delta\mu_j}{4\pi h\epsilon_0 r^3}\kappa, \tag{6}$$

where $\Delta\mu_i$ and $\Delta\mu_j$ are changes in the static dipole moment between the ground and the excited state of the candidate qubit and readout ions, respectively. h is the Planck's constant, ϵ_0 is the permittivity of vacuum, r is the separation between the two ions and κ quantifies the angular dependence of the interaction. The change in the dipole moment between the ground and the excited states has been measured for Pr^{3+} ions [52]. For two Pr^{3+} ions separated by ∼5 nm, which is the average ion-ion distance at 500 ppm doping concentration, a frequency shift of ∼10 MHz is expected. In addition, dipole interaction has been experimentally investigated between Ce^{3+} and Pr^{3+} in Y_2SiO_5 and was found to be in the order of 300 MHz for ions separated by ∼5 nm [53]. This can be used as an-order-of magnitude estimate of the expected frequency shift between the Nd^{3+} ion and Pr^{3+} ion here. It should be noted here that the doping concentration of the qubit ion can be optimized such that there is an abundance of qubit ions strongly interacting with the readout ions. In our case, the higher concentration of Pr^{3+} increases the chance of having strongly interacting qubit ions in proximity to the readout ions, which is necessary for the dipole blockade mechanism to work [8,54]. It could, however, be challenging to resolve a single readout ion in a sample with a 100 ppm doping concentration. To tackle this issue, lower doping concentration < 1 ppm can be considered for the readout application. Given the data we measured and using a reasonable assumption of the dipole interaction shift, it would be useful to evaluate how good the Nd^{3+} ion will perform in terms of readout fidelity. When coupling an emitter to a cavity, the emitter's excited state lifetime is reduced to $T_c = T_1/(C+1)$, where T_1 is the natural lifetime, T_c is the Purcell enhanced lifetime, and C is the Purcell factor given by [55]

$$C = \zeta \frac{3\lambda^3}{4\pi^2}\frac{Q}{V_m}, \tag{7}$$

where λ is the emission wavelength, Q the quality factor of the resonator, V_m its mode volume, and ζ the branching ratio of the respective transition.

Nanoparticles that are investigated in this work are well suited to be integrated into fiber-based microcavities. However, scattering losses due to the particles are one of the key challenges to obtain high Q values. In particular, for the 380 nm Nd^{3+}-doped particles, the expected scattering loss is ∼8% per pass at 892 nm wavelength. Particles of 80 nm size have been realized [28], and if we instead consider those, scattering losses will be reduced to ∼5 ppm. At this level, a loaded cavity finesse of 3×10^5 could be obtained using cavity mirrors with a total transmission of 10 ppm [56]. For a loaded cavity with such a finesse, a $Q \sim 2 \times 10^6$ and $V_m \sim 5\lambda^3$ can be reached. From Eq. (7), this corresponds to a Purcell enhancement $C \sim 5000$ and an enhanced lifetime of $T_c \sim 100$ ns. Similarly, a $Q \sim 10^5$ and $V_m \sim 5\lambda^3$ can be reached for a cavity loaded with the 150 nm Er^{3+}-doped particles investigated here using similar cavity mirrors. Reducing the particle size to 100 nm would reduce the scattering losses and consequently increase Q by a factor of 3. Assuming an open cavity with those parameters, this would give $C \sim 5500$ and $T_c \sim 2.5$ μs for Er^{3+}. To reduce Er^{3+} excited-state lifetime down to ∼100 ns, which is needed to obtain fast and reliable readout at a timescale comparable to the gate operation time as discussed earlier, a finesse of 4×10^6 and a cavity length of ∼1λ will be required, which is quite challenging to obtain. Here, we will only consider Nd^{3+} as a candidate readout ion with its 100 ns achievable enhanced lifetime.

Assuming an open cavity with the parameters discussed above, this would yield an enhanced lifetime of 100 ns for the envisioned readout ion Nd^{3+}. A detection rate of 10^6

photons/s would be expected, given a reasonable assumption of 10% for the optical efficiency. Since the fiber is used both as a cavity mirror and as an outcoupler, a high collection efficiency would be expected, limited mainly by mode mismatching between the cavity and the fiber.

Debnath *et al.* proposed a protocol based on Bayesian analysis of the detected photons from a readout ion to extract information about the state of the qubit ion [57]. In this protocol, the detection rate (1 MHz in our case) replaces the decay rate. To estimate the readout fidelity of our system based on this protocol, we assume an interaction shift (dipole blockade) of about 5 MHz compared to the estimated 1.6 MHz homogeneous linewidth of the cavity enhanced lifetime of 100 ns. Considering a qubit excited-state emission rate of ∼140 times the detection rate ($T_1 \sim 140\,\mu$s was measured for Pr^{3+}:Y_2O_3 [26]), the protocol estimates a readout fidelity of ∼94% after about 10 μs. As discussed above, an interaction shift of 10–100 MHz is consistent with a shift between ions separated by a few nanometers, which is a typical separation between RE ions at our doping concentrations. If we consider Eu^{3+} as a candidate qubit instead, with an excited-state lifetime of ∼2 ms, the fidelity scales up to ∼99% after 10 μs [15]). This fidelity is limited by the finite lifetime of the qubit ion, since if it decays spontaneously during the detection, it will cause a loss of the state information. However, this problem can be mitigated by using one qubit as a dedicated buffer to the readout ions, to which the state of any other qubit that should be readout can be transferred as described in detail in Ref. [49]. This way, the state information of the qubit will be protected from decay events by the buffer ion. By cycling a few times between the qubit and the buffer ion, the readout fidelity can be improved significantly to 99.9%. This would be at the cost of extending the detection duration to ∼25-40 μs, only limited by the qubit decay during the transfer pulses for projecting the qubit state onto the buffer ion.

B. Source of Fourier-limited single photons

Single erbium ions would be ideal candidates for use as quantum nodes in a quantum network due to their emission at telecommunication wavelengths. Furthermore, erbium ions that are spatially close to each other in the solid-state matrix allow for multiqubit operations, which is highly desirable in a quantum network. A key requirement for using single emitters as quantum nodes is that the emitted photons should be indistinguishable. In the spectral domain, this means that the photons should be Fourier-transform limited. To extract Fourier-limited photons from a single erbium ion, we need to have $T_2 = 2T_1$, where T_1 is the lifetime of the excited state, and T_2 is the coherence time. For the values we have measured for Er^{3+} : Y_2O_3 nanoparticles in this paper at a temperature of 3 K, which is $T_1 = 13.7$ ms and $T_2 = 839$ ns, we have $T_2 \ll 2T_1$. For measurements in quantum networks where photons from different remote erbium emitters have to interfere at a beam splitter, it is not only necessary that the instantaneous linewidth is lifetime limited but also that the central frequency does not drift such that the frequency overlap between the two photons remains high. This means that long-term spectral diffusion effects have to be taken into account, such that the relevant parameter would be in that case T_2^*. Note, however, that slow drifts could be compensated for using, e.g., external electric fields.

To satisfy the condition for indistinguishable photons, we would need to either increase T_2 (or T_2^*) or decrease T_1. As discussed above, the T_2 at low temperatures in the current samples is limited due to spectral diffusion arising from coupling to neighboring TLSs. TLS behavior is characteristic of amorphous materials [45], and could be arising in our system due to the presence of defects and the poor crystalline quality of our nanoparticles. As the contribution from TLSs to homogeneous linewidth depends on temperature, coherence times can be significantly improved by cooling the samples further. In our current samples, the homogeneous linewidth reduces by 121 kHz per kelvin and reaches a value of 10 kHz ($T_2 \approx 32\,\mu$s) when extrapolated to 0 K. The effect of TLSs can also be minimized by annealing the samples at high temperatures (>1200 °C), but this also leads to an increase in the average size of our nanoparticles, which would make it difficult to integrate them into microcavities due to higher scattering losses. An alternative method that involves starting with bigger higher quality nanoparticles and then chemically etching them down to the required size has shown promising results [24]. By chemically etching 400 nm Y_2O_3 nanoparticles doped with europium down to 150 nm, they were able to demonstrate a T_2 of 10 μs. Recent results obtained with Y_2O_3 ceramics at mK temperatures have shown a sub kHz optical homogeneous linewidth [25].

Nonetheless, it is clear that both for the purpose of producing indistinguishable photons and also for making the emission efficient, we would need to additionally reduce the T_1. This can be achieved by coupling the emitter to an optical cavity and utilizing the Purcell effect as described above in Eq. (7) [28]. The Er^{3+} : Y_2O_3 nanoparticles investigated in this paper with an average size of 150 nm introduce a scattering loss of ≈35 ppm. To efficiently extract photons emitted by ions in our nanoparticle coupled to a microcavity, this scattering loss needs to be smaller than all other losses in the cavity. For instance, our current nanoparticles can be efficiently coupled to cavities with $Q \sim 10^6$ and $V_m \sim 5\,\lambda^3$. Using a lower bound $\zeta > 0.13$ as measured in this paper, we expect a Purcell enhancement $C > 2000$, which corresponds to $T_c < 7\,\mu$s. To produce indistinguishable photons, we would then need $T_2 \sim 14\,\mu$s, which could be achieved both by improved sample fabrication as well as by cooling the samples further. Alternately, if the nanoparticles can be made with an average diameter of ≈100 nm, then the scattering losses drop to ≈4 ppm, in which case it would be possible to use cavities with $Q \sim 10^7$ that would result in $C \sim 20\,000$ and $T_c \sim 700$ ns. In this case, $T_2 \sim 1.4\,\mu$s would be sufficient to produce indistinguishable photons, which could be reached with the samples studied in this paper by cooling them to ∼1.5 K.

V. CONCLUSION

We have investigated the optical coherence properties of Er^{3+} and Nd^{3+} in Y_2O_3 ceramics and nanoparticles at cryogenic temperatures. An inhomogeneous linewidth of 10.7 GHz and 8.2 GHz were measured for the $^4I_{13/2} - {}^4I_{15/2}$ transition in Er^{3+} and $^4F_{3/2} - {}^4I_{9/2}$ transition in Nd^{3+}, respectively. Furthermore, the lifetime of the excited for the two transitions was measured to be 13.68 ms and 540 μs for the two aforementioned transitions, respectively. The two-pulse technique method was used to measure

the homogeneous linewidth for the two ions at different temperatures. For Er^{3+} transition, a homogeneous linewidth of 379 kHz was measured at a base temperature of 3 K, while a linewidth of 62 kHz was measured in Nd^{3+} at a base temperature of 1.6 K. Time-dependent broadening of the homogeneous linewidth due to spectral diffusion was investigated in Er^{3+} using 3PPE technique, and a TLS coupling constant of 2.3 MHz was obtained.

Finally, we propose two quantum applications, single qubit-state readout and a Fourier-limited single photon source, for which the investigated ion are expected to perform well when combined with fiber-based microcavities, where a strong Purcell enhancement can be reached. To reach the necessary Purcell enhancement levels, cavities with a quality factor in the range of 10^6–10^7 and a mode volume in the order of $\sim 5\,\lambda^3$ are required.

ACKNOWLEDGMENTS

This research was supported by the European Union's Horizon 2020 research and innovation program No. 712721 (NanOQTech), and the European Union FETFLAG program Grant No. 820391 (SQUARE), the Swedish Research Council (2021-03755), the Wallenberg Center for Quantum Technology (WACQT) funded by the Knut and Alice Wallenberg Foundation (KAW 2017.0449). ICFO acknowledges financial support from the government of Spain (PID 2019-106850RB-I00 (QRN) and Severo Ochoa CEX2019-000910-S, funded by MCIN/AEI/10.13039/501100011033), from MCIN with funding from European Union NextGenerationEU (PRTR-C17.I1), from Fundació Cellex, Fundació Mir-Puig, and from Generalitat de Catalunya (CERCA, AGAUR).

[1] M. P. Hedges, J. J. Longdell, Y. Li, and M. J. Sellars, Nature **465**, 1052 (2010).
[2] T. Zhong, J. M. Kindem, J. G. Bartholomew, J. Rochman, I. Craiciu, E. Miyazono, M. Bettinelli, E. Cavalli, V. Verma, S. W. Nam, F. Marsili, M. D. Shaw, A. D. Beyer, and A. Faraon, Science **357**, 1392 (2017).
[3] A. Seri, A. Lenhard, D. Rieländer, M. Gündoğan, P. M. Ledingham, M. Mazzera, and H. de Riedmatten, Phys. Rev. X **7**, 021028 (2017).
[4] A. Ortu, A. Holzäpfel, J. Etesse, and M. Afzelius, npj Quantum Inf. **8**, 29 (2022).
[5] J. J. Longdell, M. J. Sellars, and N. B. Manson, Phys. Rev. Lett. **93**, 130503 (2004).
[6] P. Goldner, A. Ferrier, and O. Guillot-Noël, in *Handbook on the Physics and Chemistry of Rare Earths*, edited by J.-C. G. Bünzli and V. K. Pecharsky (Elsevier, 2015), Vol. 46, pp. 1–78.
[7] R. L. Ahlefeldt, M. J. Pearce, M. R. Hush, and M. J. Sellars, Phys. Rev. A **101**, 012309 (2020).
[8] A. Kinos, L. Rippe, D. Serrano, A. Walther, and S. Kröll, Phys. Rev. A **105**, 032603 (2022).
[9] M. J. Thorpe, L. Rippe, T. M. Fortier, M. S. Kirchner, and T. Rosenband, Nat. Photon. **5**, 688 (2011).
[10] C. L. Degen, F. Reinhard, and P. Cappellaro, Rev. Mod. Phys. **89**, 035002 (2017).
[11] J. G. Bartholomew, J. Rochman, T. Xie, J. M. Kindem, A. Ruskuc, I. Craiciu, M. Lei, and A. Faraon, Nat. Commun. **11**, 3266 (2020).
[12] L. A. Williamson, Y.-H. Chen, and J. J. Longdell, Phys. Rev. Lett. **113**, 203601 (2014).
[13] R. W. Equall, Y. Sun, R. L. Cone, and R. M. Macfarlane, Phys. Rev. Lett. **72**, 2179 (1994).
[14] C. W. Thiel, T. Böttger, and R. L. Cone, J. Lumin. **131**, 353 (2011).
[15] M. Zhong, M. P. Hedges, R. L. Ahlefeldt, J. G. Bartholomew, S. E. Beavan, S. M. Wittig, J. J. Longdell, and M. J. Sellars, Nature **517**, 177 (2015).
[16] F. K. Asadi, N. Lauk, S. Wein, N. Sinclair, C. O'Brien, and C. Simon, Quantum **2**, 93 (2018).
[17] D. P. DiVincenzo, Fortschr. Phys. **48**, 771 (2000).
[18] A. M. Dibos, M. Raha, C. M. Phenicie, and J. D. Thompson, Phys. Rev. Lett. **120**, 243601 (2018).
[19] S. Chen, M. Raha, C. M. Phenicie, S. Ourari, and J. D. Thompson, Science **370**, 592 (2020).
[20] T. Zhong, J. M. Kindem, J. G. Bartholomew, J. Rochman, I. Craiciu, V. Verma, S. W. Nam, F. Marsili, M. D. Shaw, A. D. Beyer, and A. Faraon, Phys. Rev. Lett. **121**, 183603 (2018).
[21] J. M. Kindem, A. Ruskuc, J. G. Bartholomew, J. Rochman, Y. Q. Huan, and A. Faraon, Nature **580**, 201 (2020).
[22] B. Casabone, J. Benedikter, T. Hümmer, F. Oehl, K. de Oliveira Lima, T. W. Hänsch, A. Ferrier, P. Goldner, H. de Riedmatten, and D. Hunger, New J. Phys. **20**, 095006 (2018).
[23] N. Harada, A. Ferrier, D. Serrano, M. Persechino, E. Briand, R. Bachelet, I. Vickridge, J.-J. Ganem, P. Goldner, and A. Tallaire, J. Appl. Phys. **128**, 055304 (2020).
[24] S. Liu, A. Fossati, D. Serrano, A. Tallaire, A. Ferrier, and P. Goldner, ACS Nano **14**, 9953 (2020).
[25] R. Fukumori, Y. Huang, J. Yang, H. Zhang, and T. Zhong, Phys. Rev. B **101**, 214202 (2020).
[26] D. Serrano, C. Deshmukh, S. Liu, A. Tallaire, A. Ferrier, H. de Riedmatten, and P. Goldner, Phys. Rev. B **100**, 144304 (2019).
[27] J. G. Bartholomew, K. de Oliveira Lima, A. Ferrier, and P. Goldner, Nano Lett. **17**, 778 (2017).
[28] B. Casabone, C. Deshmukh, S. Liu, D. Serrano, A. Ferrier, T. Hümmer, P. Goldner, D. Hunger, and H. de Riedmatten, Nat. Commun. **12**, 3570 (2021).
[29] P. Jobez, N. Timoney, C. Laplane, J. Etesse, A. Ferrier, P. Goldner, N. Gisin, and M. Afzelius, Phys. Rev. A **93**, 032327 (2016).
[30] C. Laplane, P. Jobez, J. Etesse, N. Gisin, and M. Afzelius, Phys. Rev. Lett. **118**, 210501 (2017).
[31] A. Ruskuc, C.-J. Wu, J. Rochman, J. Choi, and A. Faraon, Nature **602**, 408 (2022).
[32] X. Fernandez-Gonzalvo, Y.-H. Chen, C. Yin, S. Rogge, and J. J. Longdell, Phys. Rev. A **92**, 062313 (2015).

[33] G. Dold, C. W. Zollitsch, J. O'Sullivan, S. Welinski, A. Ferrier, P. Goldner, S. E. de Graaf, T. Lindström, and J. J. L. Morton, Phys. Rev. Appl. **11**, 054082 (2019).
[34] Y. Sun, C. W. Thiel, R. L. Cone, R. W. Equall, and R. L. Hutcheson, J. Lumin. **98**, 281 (2002).
[35] X. Cui, J. Lu, C. Gao, C. Hou, W. Wei, and B. Peng, Appl. Phys. A **103**, 27 (2011).
[36] K. de Oliveira Lima, R. R. Gonçalves, D. Giaume, A. Ferrier, and P. Goldner, J. Lumin. **168**, 276 (2015).
[37] J. B. Gruber, R. P. Leavitt, C. A. Morrison, and N. C. Chang, J. Chem. Phys. **82**, 5373 (1985).
[38] B. M. Walsh, J. M. McMahon, W. C. Edwards, N. P. Barnes, R. W. Equall, and R. L. Hutcheson, J. Opt. Soc. Am. B **19**, 2893 (2002).
[39] D. Serrano, J. Karlsson, L. Zheng, Y. Dong, A. Ferrier, P. Goldner, A. Walther, L. Rippe, and S. Kröll, J. Lumin. **170**, 102 (2016).
[40] N. C. Chang, J. B. Gruber, R. P. Leavitt, and C. A. Morrison, J. Chem. Phys. **76**, 3877 (1982).
[41] R. M. Macfarlane, J. Lumin. **100**, 1 (2002).
[42] I. N. Kurkin and K. P. Chernov, Physica B+C **101**, 233 (1980).
[43] P. L. Scott and C. D. Jeffries, Phys. Rev. **127**, 32 (1962).
[44] T. Böttger, C. W. Thiel, Y. Sun, and R. L. Cone, Phys. Rev. B **73**, 075101 (2006).
[45] L. Veissier, M. Falamarzi, T. Lutz, E. Saglamyurek, C. W. Thiel, R. L. Cone, and W. Tittel, Phys. Rev. B **94**, 195138 (2016).
[46] B. Car, L. Veissier, A. Louchet-Chauvet, J.-L. Le Gouët, and T. Chanelière, Phys. Rev. Lett. **120**, 197401 (2018).
[47] B. Car, J.-L. Le Gouët, and T. Chanelière, Phys. Rev. B **102**, 115119 (2020).
[48] W. A. Phillips, J. Low Temp. Phys. **7**, 351 (1972).
[49] A. Walther, L. Rippe, Y. Yan, J. Karlsson, D. Serrano, A. N. Nilsson, S. Bengtsson, and S. Kröll, Phys. Rev. A **92**, 022319 (2015).
[50] A. Kinos, L. Rippe, S. Kröll, and A. Walther, Phys. Rev. A **104**, 052624 (2021).
[51] S. B. Altner, G. Zumofen, U. P. Wild, and M. Mitsunaga, Phys. Rev. B **54**, 17493 (1996).
[52] F. R. Graf, A. Renn, G. Zumofen, and U. P. Wild, Phys. Rev. B **58**, 5462 (1998).
[53] Y. Yan, J. Karlsson, L. Rippe, A. Walther, D. Serrano, D. Lindgren, M.-e. Pistol, S. Kröll, P. Goldner, L. Zheng, and J. Xu, Phys. Rev. B **87**, 184205 (2013).
[54] A. Kinos, D. Hunger, R. Kolesov, K. Mølmer, H. de Riedmatten, P. Goldner, A. Tallaire, L. Morvan, P. Berger, S. Welinski, K. Karrai, L. Rippe, S. Kröll, and A. Walther, arXiv:2103.15743.
[55] E. M. Purcell, Phys. Rev. **69**, 674 (1946).
[56] F. Rochau, I. Sánchez Arribas, A. Brieussel, S. Stapfner, D. Hunger, and E. M. Weig, Phys. Rev. Appl. **16**, 014013 (2021).
[57] K. Debnath, A. H. Kiilerich, and K. Mølmer, Phys. Rev. A **103**, 043705 (2021).